HARM3D+NUC: A New Method for Simulating the Post-merger Phase of Binary Neutron Star Mergers with GRMHD, Tabulated EOS, and Neutrino Leakage

Ariadna Murguia-Berthier[1,2] , Scott C. Noble[3] , Luke F. Roberts[4], Enrico Ramirez-Ruiz[1,2] , Leonardo R. Werneck[5], Michael Kolacki[6,7], Zachariah B. Etienne[5,8], Mark Avara[9], Manuela Campanelli[7,9,10] , Riccardo Ciolfi[11,12] , Federico Cipolletta[13], Brendan Drachler[7,14], Lorenzo Ennoggi[9], Joshua Faber[7,9,10], Grace Fiacco[7,14], Bruno Giacomazzo[15,16,17] , Tanmayee Gupte[7,14], Trung Ha[14], Bernard J. Kelly[3,18,19] , Julian H. Krolik[20] , Federico G. Lopez Armengol[14] , Ben Margalit[21] , Tim Moon[9,10], Richard O'Shaughnessy[7,9,10] , Jesús M. Rueda-Becerril[9], Jeremy Schnittman[3], Yossef Zenati[20], and Yosef Zlochower[7,9,10]

[1] Department of Astronomy and Astrophysics, University of California, Santa Cruz, CA 95064, USA
[2] DARK, Niels Bohr Institute, University of Copenhagen, Blegdamsvej 17, DK-2100 Copenhagen, Denmark
[3] Gravitational Astrophysics Lab, NASA Goddard Space Flight Center, Greenbelt, MD 20771, USA
[4] NSCL, Michigan State University, East Lansing, MI 48824, USA
[5] Center for Gravitational Waves and Cosmology, West Virginia University, Chestnut Ridge Research Building, Morgantown, WV 26505, USA
[6] Center for Computational Relativity, Rochester Institute of Technology, Rochester, NY 14623, USA
[7] School of Physics and Astronomy, Rochester Institute of Technology, Rochester, NY 14623, USA
[8] Department of Physics and Astronomy, West Virginia University, Morgantown, WV 26506, USA
[9] Center for Computational Relativity and Gravitation, Rochester Institute of Technology, 85 Lomb Memorial Drive, Rochester, NY 14623, USA
[10] School of Mathematical Sciences, Rochester Institute of Technology, Rochester, NY 14623, USA
[11] INAF, Osservatorio Astronomico di Padova, Vicolo dell'Osservatorio 5, I-35122 Padova, Italy
[12] INFN, Sezione di Padova, Via Francesco Marzolo 8, I-35131 Padova, Italy
[13] Leonardo Corporate LABS—via Raffaele Pieragostini 80, I-16149 Genova GE, Italy
[14] Center for Computational Relativity and Gravitation, Rochester Institute of Technology, Rochester, NY 14623, USA
[15] Universitá degli Studi di Milano—Bicocca, Dipartimento di Fisica G. Occhialini, Piazza della Scienza 3, I-20126 Milano, Italy
[16] INFN, Sezione di Milano-Bicocca, Piazza della Scienza 3, I-20126 Milano, Italy
[17] INAF, Osservatorio Astronomico di Brera, via E. Bianchi 46, I-23807 Merate (LC), Italy
[18] Department of Physics, University of Maryland Baltimore County, 1000 Hilltop Circle Baltimore, MD 21250, USA
[19] Center for Research and Exploration in Space Science and Technology, NASA Goddard Space Flight Center, Greenbelt, MD 20771, USA
[20] Physics and Astronomy Department, Johns Hopkins University, Baltimore, MD 21218, USA
[21] Astronomy Department and Theoretical Astrophysics Center, University of California, Berkeley, Berkeley, CA 94720, USA
Received 2021 May 5; revised 2021 July 2; accepted 2021 July 2; published 2021 September 29

Abstract

The first binary neutron star merger has already been detected in gravitational waves. The signal was accompanied by an electromagnetic counterpart including a kilonova component powered by the decay of radioactive nuclei, as well as a short γ-ray burst. In order to understand the radioactively powered signal, it is necessary to simulate the outflows and their nucleosynthesis from the post-merger disk. Simulating the disk and predicting the composition of the outflows requires general relativistic magnetohydrodynamical (GRMHD) simulations that include a realistic, finite-temperature equation of state (EOS) and self-consistently calculating the impact of neutrinos. In this work, we detail the implementation of a finite-temperature EOS and the treatment of neutrinos in the GRMHD code HARM3D+NUC, based on HARM3D. We include formal tests of both the finite-temperature EOS and the neutrino-leakage scheme. We further test the code by showing that, given conditions similar to those of published remnant disks following neutron star mergers, it reproduces both recombination of free nucleons to a neutron-rich composition and excitation of a thermal wind.

Unified Astronomy Thesaurus concepts: Relativistic disks (1388); General relativity (641); Magnetohydrodynamical simulations (1966); Nuclear astrophysics (1129)

1. Introduction

On 2017 August 17, the LIGO/VIRGO collaboration detected the first gravitational wave signal arising from the merger of two neutron stars (Abbott et al. 2017a). This signal was accompanied by a counterpart observed all over the electromagnetic spectrum (Abbott et al. 2017b; Coulter et al. 2017; Murguia-Berthier et al. 2017; Shappee et al. 2017). This event, named GW170817, gave credence to the idea that at least a subset of neutron star mergers give rise to short γ-ray bursts (sGRBs; Eichler et al. 1989; Narayan et al. 1992; Lee & Ramirez-Ruiz 2007; Nakar 2007).

In order to understand the electromagnetic emission, we need to study the properties of such mergers. After the two neutron stars merge, the fate of the remnant depends on the final mass of the resulting object. If the final mass is less than the mass allowed for an object with rigid rotation, then the remnant will be a stable neutron star. On the other hand, if the final mass is larger, then it can result in a hot hypermassive neutron star (HMNS), supported by differential rotation, or it can promptly collapse to a black hole (Shibata & Taniguchi 2006; Baiotti et al. 2008; Ravi & Lasky 2014). In both cases, the compact object will be surrounded by an accretion disk (Eichler et al. 1989; Baiotti et al. 2008). If the result is an HMNS, there will be transport of mass and angular momentum from the inner edge to the outer edge that will drive the HMNS to rigid rotation, where it can either remain stable, or undergo a delayed collapse to a black hole (BH; see Nakar 2020, for a recent review). It is widely believed that GW170817 resulted in a delayed collapse to a black hole (Margalit & Metzger 2017).

In any case, the compact object is left surrounded by an accretion disk containing highly neutron-rich material (Lee & Ramirez-Ruiz 2007).

The post-merger accretion disk will be entirely opaque to photons (Popham et al. 1999; Narayan et al. 2001; Lee et al. 2004, 2005, 2009). As we go deeper in the disk, due to the high density and temperature, neutrinos (and antineutrinos) will be created via the charged β-process, electron–positron annihilation, and plasmon decay (Narayan et al. 2001; Di Matteo et al. 2002; Chen & Beloborodov 2007; Liu et al. 2017). In the region where the neutrinos are created, matter will be optically thin to neutrinos. In even deeper regions, matter will be optically thick to neutrinos. In the optically thin region, free neutrinos will carry energy away, and cool the disk, making it geometrically thinner (Chevalier 1989; Houck & Chevalier 1991).

Further out in the disk, where neutrinos are no longer created in substantial numbers, free nucleons will recombine into α-particles. The photons will still be trapped in the disk, therefore the disk will be thicker and radiatively inefficient (Popham et al. 1999; Narayan et al. 2001; Lee et al. 2004, 2005, 2009). An outflow arises due to instabilities in the accretion disk from its magnetic field (Balbus & Hawley 1998). The instabilities will transport angular momentum at significant rates, dissipating energy and driving a high-velocity outflow. In addition, the recombination of free nucleons into α-particles is capable of unbinding part of the material from the disk (Lee et al. 2009; Fernández & Metzger 2013a).

Aside from material ejected from the disk, there are other outflows from the binary merger that will significantly contribute to the electromagnetic emission, including dynamical ejecta (see, e.g., Rosswog et al. 1999; Fernández et al. 2015; Radice et al. 2016) and a neutrino-driven wind (Dessart et al. 2009; Fernández & Metzger 2013a; Perego et al. 2014; Fernández et al. 2017; Kasen et al. 2017). As the different outflows expand and cool down, heavy elements are synthesized via the rapid neutron capture process (r-process) (Freiburghaus et al. 1999; Kulkarni 2005; Fernández & Metzger 2013b; Lippuner & Roberts 2015; Palenzuela et al. 2015; Radice et al. 2016, 2018, 2020; Fernández et al. 2017; Roberts et al. 2017; Lippuner et al. 2017; Zenati et al. 2019). After neutrons are exhausted, elements will radioactively decay and heat the surrounded material, which will thermally emit in the optical/IR bands (Li & Paczyński 1998; Metzger et al. 2010; Roberts et al. 2011; Barnes & Kasen 2013; Kasen et al. 2013; Tanaka & Hotokezaka 2013; Grossman et al. 2014; Kasen et al. 2015; Barnes et al. 2016; Rosswog et al. 2017; Kasen & Barnes 2019; Siegel 2019); in particular, see Metzger (2019) and references within. This emission, called a kilonova, was detected for GW170817 (Cowperthwaite et al. 2017; Drout et al. 2017; Kilpatrick et al. 2017; Kasen et al. 2017; Nicholl et al. 2017; Pian et al. 2017; Smartt et al. 2017; Soares-Santos et al. 2017; Tanvir et al. 2017; Villar et al. 2017; Kasliwal et al. 2019). It is predicted that, if the composition of the ejecta includes lanthanides, the emission tends to be more red and peak at later times, whereas if there are no third-peak elements, the emission tends to be bluer and peaks earlier (Barnes & Kasen 2013; Tanaka & Hotokezaka 2013). Understanding the nucleosynthesis, as well as the amount of mass ejected, is therefore important when deciding the best strategy to observe and perform surveys for kilonovae. This paper will focus on the disk ejecta.

The key parameter in determining the rate of nucleosynthesis, and in particular whether third-peak r-process elements (including the lanthanides) are created in the disk ejecta, is the electron fraction of the ejected material (Kasen et al. 2013, 2017; Lippuner & Roberts 2015; Roberts et al. 2017; Lippuner et al. 2017; Just et al. 2021). The problem is that the composition of these ejecta varies between different simulations, with results ranging from compositions dominated by iron peak elements to ejecta dominated by lanthanides (e.g., Janiuk 2014; Fernández et al. 2015; Foucart et al. 2018; Siegel & Metzger 2018; Janiuk 2019; Miller et al. 2019b). One of the significant differences between the simulations is in the neutrino treatment. Neutrinos carry away energy and lepton number, altering the electron fraction and the final ejecta mass, and they significantly alter the composition of the ejected material. Thus, simulations need to model the composition and thermodynamic state of the ejecta as realistically as possible in order to understand and model the kilonova emission.

To model the post-merger disk, we need to self-consistently include multiple relevant physical processes. Due to the compact nature of the BH, we need to consider general relativity (GR). Due to the importance of the magnetic stresses, we also need to include magnetohydrodynamics (MHD). Additionally, to self-consistently include the addition of neutrinos and recombination energy, we need both a realistic equation of state (EOS) and a way in which to consider the impact of neutrinos in the optically thick and thin regions.

There have been many previous efforts to simulate a black hole surrounded by an accretion disk in the context of a binary neutron star. A brief (and certainly incomplete) summary of the numerical efforts is below.

Numerical simulations initially added neutrino physics by adding pressure terms in the EOS and adding emission and heating/cooling terms from weak reactions in hydrodynamical simulations (Popham et al. 1999; Narayan et al. 2001; Di Matteo et al. 2002; Kohri & Mineshige 2002; Lee et al. 2004, 2005; Metzger et al. 2008; Zalamea & Beloborodov 2011). There have been general relativistic magnetohydrodynamical (GRMHD) simulations in 2D with analytical terms for the neutrino pressure with approximations by Di Matteo et al. (2002) that also include nuclear reactions using the GRMHD code HARM2D (Janiuk et al. 2013; Janiuk 2014, 2019). There have been works that performed simulations of binary neutron stars, or a hypermassive NS, with an accretion disk in 3D with GRMHD but without neutrinos (for example, Kiuchi et al. 2014, 2015, 2018; Siegel et al. 2014; Dionysopoulou et al. 2015; Ruiz et al. 2016; Ciolfi et al. 2017; Ruiz et al. 2018). Also, some groups have simulated disks after the merger of binary NS including GR with some kind of neutrino transport but including no magnetic fields (Foucart et al. 2016; Fujibayashi et al. 2017; Nedora et al. 2021). Other groups have performed hydrodynamical calculations with neutrino physics, including neutrino-leakage schemes and a transport scheme but no magnetic fields (Ruffert et al. 1996; Rosswog & Liebendörfer 2003; Metzger & Fernández 2014; Perego et al. 2014; Fernández et al. 2015; Just et al. 2015; Martin et al. 2015).

Foucart et al. (2015, 2018) performed general relativistic hydrodynamical (GRHD) simulations and compared different neutrino treatments, including neutrino transport and leakage schemes. Furthermore, Siegel & Metzger (2018) and De & Siegel (2020) performed GRMHD simulations of a magnetized torus with a neutrino-leakage scheme and the Helmholtz EOS. Hossein Nouri et al. (2018) compared 3D simulations of magnetized and unmagnetized accretion disks with GRMHD including a neutrino-leakage scheme. Li & Siegel (2021)

performed an M1 scheme with neutrino conversions. There have also been GRMHD simulations that included a tabulated EOS with neutrino transport using Monte Carlo methods (Miller et al. 2019a, 2019b).

In this paper, we present simulations using HARM3D +NUC, based on HARM3D, considering the impact of neutrinos through a leakage scheme and a multicomponent, finite-temperature EOS. HARM3D is a well-tested, versatile GRMHD code that has been used in many astrophysical scenarios. It uses arbitrary coordinates, allowing for a more accurate conservation of angular momentum. In addition, it has copious analysis tools developed over the years. The addition of a neutrino-leakage scheme and tabulated EOS into HARM3D+NUC is a stepping stone that allows for further advances. The paper is structured as follows: in Section 2, we discuss how we implemented the realistic EOS and the leakage scheme. In Section 3, we describe the tests we performed to validate the implementation of the tabulated EOS, including a torus in hydrostatic equilibrium. In Section 4, we describe the tests performed to validate the leakage scheme. In Section 5, we use both the tabulated EOS and leakage scheme to better simulate a torus with a magnetic field.

2. Methods

In order to accurately simulate accretion disks, we need the ability to solve the GRMHD equations with a realistic EOS and a way to account for the effect neutrinos and antineutrinos have on the material's energy and electron fraction. In this section, we explain how we added a tabulated EOS and neutrino-leakage scheme to HARM3D, in a new code called HARM3D+NUC.

2.1. HARM3D+NUC

HARM3D (Gammie et al. 2003; Noble et al. 2006, 2009) solves the GRMHD equations in conservative form. HARM3D is a well-tested code that can handle arbitrary coordinate systems, which allows for less numerical diffusion and better conservation of angular momentum when using coordinate systems that more closely conform to local symmetries of the problem (Zilhão & Noble 2014). Below, we set $G = c = 1$. The GRMHD equations of motion include the baryon conservation equation,

$$\nabla_\mu(n_b u^\mu) = 0, \tag{1}$$

the energy–momentum conservation equations (with a heating/cooling source, neglecting momentum transfer)

$$\nabla_\mu T^\mu{}_\nu = \mathcal{Q} u_\nu, \tag{2}$$

and Maxwell's equations

$$\nabla^*_\nu F^{\mu\nu} = 0, \tag{3}$$
$$\nabla_\nu F^{\mu\nu} = J^\mu, \tag{4}$$

where u^μ is the four-velocity of the fluid, $\mathcal{Q}$ is the energy change rate per volume in the comoving fluid frame (due to neutrino heating/cooling), n_b is the number density of baryons, $F^{\mu\nu}$ is the Faraday tensor times $1/\sqrt{4\pi}$, $^*F^{\mu\nu}$ is the dual of this tensor or the Maxwell tensor times $1/\sqrt{4\pi}$, and J^μ is the four-current.[22] In practice, we do not use Equation (4), since we

---

[22] We follow Gammie et al. (2003) in our definition of the electromagnetic field tensor and magnetic field variables.

work in the limit of ideal MHD. The change in the conservation of lepton number is

$$\nabla_\mu(n_e u^\mu) = \mathcal{R}/m_b, \tag{5}$$

where n_e is the number density of electrons and $\mathcal{R} = -\mathcal{R}_{\nu_e} + \mathcal{R}_{\bar{\nu}_e}$ is the difference in the net rate of neutrino and antineutrino number per volume in the comoving fluid frame.

Note that the rest-mass density of the gas (mass per unit volume) is dominated by the baryon mass, $\rho \approx m_b n_b$, where m_b is the baryon mass. The baryon number conservation equation can then be replaced by the regular continuity equation:

$$0 = m_b \nabla_\mu(n_b u^\mu) = \nabla_\mu(m_b n_b u^\mu) = \nabla_\mu(\rho u^\mu). \tag{6}$$

Instead of using n_e and n_b, we may use the fluid density ρ and the electron fraction Y_e:

$$Y_e \equiv \frac{n_e}{n_b} = \frac{n_e}{\rho/m_b} = \frac{m_b n_e}{\rho} \tag{7}$$

or $Y_e \rho = m_b n_e$. We can therefore multiply Equation (5) by m_b to yield the electron fraction equation:

$$\nabla_\mu(\rho Y_e u^\mu) = \mathcal{R}. \tag{8}$$

The total stress-energy tensor is the sum of the fluid part,

$$T^{\mu\nu}_{\text{fluid}} = \rho h u^\mu u^\nu + P g^{\mu\nu}, \tag{9}$$

and the electromagnetic part

$$T^{\mu\nu}_{\text{EM}} = F^{\mu\lambda} F^\nu{}_\lambda - \frac{1}{4} g^{\mu\nu} F^{\lambda\kappa} F_{\lambda\kappa} \tag{10}$$

$$= ||b||^2 u^\mu u^\nu + \frac{1}{2} ||b||^2 g^{\mu\nu} - b^\mu b^\nu, \tag{11}$$

where we adopt the ideal MHD condition

$$u_\lambda F^{\lambda\kappa} = 0, \tag{12}$$

and where $g_{\mu\nu}$ is the metric, $h = (1 + \epsilon + P/\rho)$ is the specific enthalpy, P is the pressure, ϵ is the specific internal energy density, $b^\mu = {}^*F^{\nu\mu} u_\nu$ is the magnetic field four-vector, and $||b||^2 \equiv b^\mu b_\mu$ is twice the magnetic pressure P_m.

Equations (2)–(6) can be expressed in flux conservative form

$$\partial_t U(P) = -\partial_i F^i(P) + S(P), \tag{13}$$

where U is a vector of "conserved" variables, F^i are the fluxes, S is a vector of source terms, and P is the vector of primitive variables. Explicitly, these are

$$P = [\rho, \mathcal{B}^k, \tilde{u}^i, Y_e, T]^T \tag{14}$$

$$U(P) = \sqrt{-g} [\rho u^t, T^t{}_t + \rho u^t, T^t{}_j, B^k, \rho Y_e u^t]^T \tag{15}$$

$$F^i(P) = \sqrt{-g} [\rho u^i, T^i{}_t + \rho u^i, T^i{}_j, (b^i u^k - b^k u^i), \rho Y_e u^i]^T \tag{16}$$

$$S(P) = \sqrt{-g} [0, T^\kappa{}_\lambda \Gamma^\lambda{}_{t\kappa} + \mathcal{Q} u_t, T^\kappa{}_\lambda \Gamma^\lambda{}_{j\kappa} + \mathcal{Q} u_i, 0, \mathcal{R}]^T, \tag{17}$$

where g is the determinant of the metric, $\Gamma^\lambda{}_{\mu\kappa}$ is the metric's affine connection, T is the temperature, and $B^i = \mathcal{B}^i/\alpha = {}^*F^{it}$ is the magnetic field.

The primitive velocity is the flow's four-velocity projected into a frame moving orthogonal to the space-like hypersurface:

$$\tilde{u}^\mu = (\delta^\mu{}_\nu + n^\mu n_\nu) u^\nu, \tag{18}$$

which only has spatial coefficients

$$\tilde{u}^i = u^i + \alpha\gamma g^{ti}, \tag{19}$$

where $\alpha = 1/\sqrt{-g^{tt}}$ is the lapse function, $\beta^i = -g^{ti}/g^{tt}$ is the shift function, $\gamma = \alpha u^t$ is the Lorentz factor, and n^μ is the four-velocity of the orthogonal frame: $n_\mu = [-\alpha, 0, 0, 0]$ and $n^\mu = [1/\alpha, -\beta^i/\alpha]^T$. Defining a fluid three-velocity $v^i = \tilde{u}^i/\gamma$, it can be shown that $\gamma = 1/\sqrt{1-v^2}$, where $v^2 = v_i v^i$.

2.2. Implementation of a Tabulated EOS in HARM3D+NUC

In the following section, we describe the implementation of a tabulated EOS in HARM3D+NUC.

The tables and routines for interpolating tabulated quantities are provided by[23] O'Connor & Ott (2010) and Schneider et al. (2017). The finite-temperature tables give thermodynamic variables, including, for example, the sound speed, as well as the chemical potentials of the nucleons, electrons/positrons and neutrinos/antineutrinos, as a function of the temperature (T), the electron fraction (Y_e), and the rest-mass density (ρ). The linear interpolation routines are provided by O'Connor & Ott (2010) and Schneider et al. (2017). The interpolation is done in $\log T$, $\log \rho$, Y_e space for $\log \epsilon$, $\log P$, and the rest of the thermodynamical variables.

The tables consider an interpolation between a single nucleus approximation (SNA) in the high-density regime and nuclear statistical equilibrium (NSE) of several nuclides in the low-density regime. The SNA is composed of free nucleons, electrons, positrons, α-particles, and photons. In the high-density regime, nuclei are included using the liquid drop model. The regimes are smoothly interpolated. Using the tables, we have the advantage that the nuclear binding energy release due to recombination energy from the α-particles is included.

There are three main calls to the EOS in HARM3D+NUC:

1. We call the EOS when setting the characteristic velocity in order to solve the Riemann problem (Gammie et al. 2003). The wave velocities depend on the relativistic sound speed (Gammie et al. 2003), which can be interpolated directly from the tables.
2. We replaced the primitive variable $u = \rho\epsilon$ with the temperature as a reconstructed variable, which makes the interpolation of the pressure faster because all independent variables are known and can be used to perform the interpolation immediately. This means that we call the EOS to obtain the primitive energy density u after we update ρ, T, and Y_e from the conservation equations.
3. We call the EOS repeatedly when converting from conserved variables to primitive variables.

Our implementation of a tabulated EOS into the conserved to primitive variables routine in HARM3D+NUC follows Siegel et al. (2018).

2.2.1. Primary Recovery: 3D Routine

The primary recovery routine follows a three-parameter root-finding method similar to ones implemented in Cerdá-Durán et al. (2008) and Siegel et al. (2018). We call this routine

the "3D" routine. For this routine, we reduce the GRMHD equations into three equations that have three unknowns, allowing us to solve the following system:

$$\tilde{Q}^2 = \left(1 - \frac{1}{\gamma^2}\right)(\mathcal{B}^2 + W)^2 - \frac{(Q_\mu\mathcal{B}^\mu)^2(\mathcal{B}^2 + 2W)}{W^2} \tag{20}$$

$$Q_\mu n^\mu = -\frac{\mathcal{B}^2}{2}\left(2 - \frac{1}{\gamma^2}\right) + \frac{(Q_\mu\mathcal{B}^\mu)^2}{2W^2} - W + P(\rho, Y_e, T) \tag{21}$$

$$\epsilon = \epsilon(\rho, Y_e, T). \tag{22}$$

Using these equations, we perform Newton–Raphson iterations until we obtain sufficiently accurate values for the independent variables γ, T, and W. Here, $Q_\mu = -n_\nu T_\mu^\nu = \alpha T_\mu^t$, and W is related to the specific enthalpy through $W = h\rho\gamma^2$.

$\tilde{Q}^\mu = j^\mu_{\ \nu}Q^\nu$, $j_{\mu\nu} = g_{\mu\nu} + n_\mu n_\nu$, and P is the pressure interpolated from tables.

2.2.2. Backup Recovery 1: 2D Routine

We also implemented backup routines that recover the conserved variables. One of them follows an optimized version of the "2D" method of Noble et al. (2006). We call this routine the "2D" routine. In this routine, the independent variables are W and v^2, found using Equations (20)–(21). We use the previous time step's set of primitive variables as initial guesses to the Newton–Raphson procedure. As was done in Siegel et al. (2018), we obtain the pressure and the temperature for each W and v^2. This is done by first constructing the specific enthalpy: $h = W/(\gamma^2\rho)$, which can also be constructed with quantities from the EOS tables: $h(\rho, T, Y_e)$. Then, with the density, the electron fraction and the specific enthalpy, we perform a Newton–Raphson method to obtain the temperature from the tables, solving the equation: $h = h(\rho, T, Y_e)$. Note that this inversion is time-expensive, which is why this routine is slower than the 3D routine.

2.2.3. Backup Recovery 2: 2D "Safe-guess" Routine

If there is non-convergence for this backup routine, we include an initial "safe guess" as described in Cerdá-Durán et al. (2008). We call this routine the "2D safe guess" routine. In this scenario, we use the upper limits of the EOS table to obtain the maximum thermodynamical quantities:

$$\rho_{\text{max}} = D, \tag{23}$$

$$T_{\text{max}} = T_{\text{max,tables}}, \tag{24}$$

$$P_{\text{max}} = P(\rho_{\text{max}}, Y_e, T_{\text{max}}). \tag{25}$$

Here, D is the density measured in the orthogonal frame:

$$D \equiv -\rho n_\mu u^\mu = \gamma\rho. \tag{26}$$

Then we can estimate the initial "safe guess" for the root-finding procedure:

$$\gamma_{\text{guess}} = \gamma_{\text{max}} = 50, \tag{27}$$

$$W_{\text{guess}} = Q_\mu n^\mu + P_{\text{max}} - \frac{\mathcal{B}^2}{2}. \tag{28}$$

---

[23] The link to the tabulated EOS is the following: https://stellarcollapse.org/SROEOS.html, and the link to the interpolation routines is: https://bitbucket.org/zelmani/eosdrivercxx/src.

2.2.4. Backup Recovery 3: 2D Dog Leg Routine

If the "safe guess" option does not converge, this routine includes a backup root-finding method: a trust-region, dog leg routine that is more robust than a Newton–Raphson (Press et al. 1992; Powell 1970). We call this routine the "2D dog leg" routine.

2.2.5. Backup Recovery 4: "Palenzuela" Routine

If all else fails, we use the routine described in Palenzuela et al. (2015). This routine solves a 1D equation using the Brent method. In this routine, called "Palenzuela," the independent variable is a rescaled variable

$$x_{\rm pal} \equiv \frac{\rho h \gamma^2}{\rho \gamma}. \tag{29}$$

We use the auxiliary rescaled variables:

$$q_{\rm pal} \equiv \frac{-(Q_\mu n^\mu + D)}{D}, \quad r_{\rm pal} \equiv \frac{\tilde{Q}^2}{D^2}, \tag{30}$$

$$s_{\rm pal} \equiv \frac{\mathcal{B}^2}{D}, \quad t_{\rm pal} \equiv \frac{Q_\mu \mathcal{B}^\mu}{D^{3/2}}. \tag{31}$$

The independent variable should be bracketed between

$$1 + q_{\rm pal} - s_{\rm pal} > x_{\rm pal} > 2 \; + \; 2q_{\rm pal} - s_{\rm pal}. \tag{32}$$

The method uses an initial guess for $x_{\rm pal}$ from the previous time step and gets approximate quantities. Using them, it updates $x_{\rm pal}$ and iterates again until convergence is reached. The method is the following (where approximate quantities will be denoted by a hat).

We obtain an approximate Lorentz factor $\hat{\gamma}^{-2}$:

$$\hat{\gamma}^{-2} = 1 - \frac{x_{\rm pal}^2 r_{\rm pal} + (2x_{\rm pal} + s_{\rm pal}) t_{\rm pal}^2}{x_{\rm pal}^2 (x_{\rm pal} + s_{\rm pal})^2}. \tag{33}$$

With that, we can estimate

$$\hat{\rho} = \frac{D}{\hat{\gamma}} \tag{34}$$

and an approximate specific energy:

$$\hat{\epsilon} = \hat{\gamma} - 1 + \frac{x_{\rm pal}}{\hat{\gamma}} (1 - \hat{\gamma}^2) + \hat{\gamma} \left(q_{\rm pal} - s_{\rm pal} + \frac{t_{\rm pal}^2}{2x_{\rm pal}^2} + \frac{s_{\rm pal}}{2\hat{\gamma}^2} \right). \tag{35}$$

A call to the EOS will give the pressure $\hat{P}(\hat{\rho}, \hat{\epsilon}, Y_e)$, and with all those approximate quantities, we can solve for $x_{\rm pal}$ using the Brent method by solving

$$0 = f(x_{\rm pal}) = x_{\rm pal} - \hat{\gamma} \left(1 + \hat{\epsilon} + \frac{\hat{P}}{\hat{\rho}} \right). \tag{36}$$

We repeat the estimation of all the hat quantities until the solution for $x_{\rm pal}$ converges.

2.3. Neutrino Leakage Scheme

In the following section, we describe how we implemented a leakage scheme that takes into account the heating/cooling due to neutrinos, as well as how their emission and absorption affect the electron fraction. This leakage scheme is suited to describe the contribution of neutrinos to the composition and energy.

2.3.1. Rates

The scheme calculates the absorption/emission rate as well as the energy-loss rates due to neutrinos. We use these rates in the source terms of Equations (2) and (5). The scheme uses energy-averaged quantities.

Like Ruffert et al. (1996), Galeazzi et al. (2013), Siegel & Metzger (2018), we consider the following neutrino reactions, each with their own absorption/emission rate (which has units of cm^{-3} s^{-1}), and the energy-loss rate due to neutrinos (with units of erg cm^{-3} s^{-1}):

1. Charged β-process with $\mathcal{R}_{\nu_i}^\beta$ and $\mathcal{Q}_{\nu_i}^\beta$:

$$e^- + p \rightarrow n + \nu_e \tag{37}$$

$$e^+ + n \rightarrow p + \bar{\nu}_e \tag{38}$$

2. Plasmon decay with $\mathcal{R}_{\nu_i}^\gamma$ and $\mathcal{Q}_{\nu_i}^\gamma$:

$$\gamma \rightarrow \nu_e + \bar{\nu}_e \tag{39}$$

$$\gamma \rightarrow \nu_x + \bar{\nu}_x, \tag{40}$$

where x is the muon and tauon, and in this case, γ corresponds to a photon.

3. Electron–positron pair annihilation with $\mathcal{R}_{\nu_i}^{ee}$ and $\mathcal{Q}_{\nu_i}^{ee}$

$$e^- + e^+ \rightarrow \nu_e + \bar{\nu}_e \tag{41}$$

$$e^- + e^+ \rightarrow \nu_x + \bar{\nu}_x. \tag{42}$$

Using the above reactions, we calculate the total number emission in the optically thin regime from species i as (Ruffert et al. 1996)

$$\mathcal{R}_{\nu_i} = \mathcal{R}_{\nu_i}^\beta + \mathcal{R}_{\nu_i}^\gamma + \mathcal{R}_{\nu_i}^{ee}, \tag{43}$$

and the total energy-loss rate in the optically thin regime is

$$\mathcal{Q}_{\nu_i} = \mathcal{Q}_{\nu_i}^\beta + \mathcal{Q}_{\nu_i}^\gamma + \mathcal{Q}_{\nu_i}^{ee}, \tag{44}$$

where "i" denotes the different neutrino/antineutrino flavors: electron, or muon and tauon.

The total emission/absorption rates and the energy-loss rates are given by an interpolation between the diffusive optically thick regime and the transparent optically thin regime (Ruffert et al. 1996):

$$\mathcal{R}_{\nu_i}^{\rm eff} = \mathcal{R}_{\nu_i} \left(1 + \frac{t_{\rm diff}}{t_{\rm emission, \mathcal{R}}} \right)^{-1} \tag{45}$$

$$\mathcal{Q}_{\nu_i}^{\rm eff} = \mathcal{Q}_{\nu_i} \left(1 + \frac{t_{\rm diff}}{t_{\rm emission, \mathcal{Q}}} \right)^{-1}. \tag{46}$$

Here, the diffusion timescale is given by

$$t_{\rm diff} = \frac{D_{\rm diff} \tau^2}{c \kappa_{\nu_i}}, \tag{47}$$

where $D_{\rm diff} = 6$ (Rosswog & Liebendörfer 2003; O'Connor & Ott 2010; Siegel & Metzger 2018), τ is the optical depth, and κ_{ν_i} is the energy-averaged opacity (in units of cm^{-1}) of ν_i. The absorption/emission and energy loss timescales are $t_{\rm emission, \mathcal{R}} = \mathcal{R}_{\nu_i}/n_{\nu_i}$, with n_{ν_i} being the neutrino number density (at chemical equilibrium), and $t_{\rm emission, \mathcal{Q}} = \mathcal{Q}_{\nu_i}/\varepsilon_{\nu_i}$, with ε_{ν_i} being the neutrino energy density. In the optically thick regime, the neutrino-loss rate is less than the diffusion time, which results in $\mathcal{R}_{\nu_i}^{\rm eff} = n_{\nu_i}/t_{\rm diff}$ and $\mathcal{Q}_{\nu_i}^{\rm eff} = \varepsilon_{\nu_i}/t_{\rm diff}$, whereas in the optically

thin regime, we recover the rates from Equations (43) and (44). The rates for the muon and tauon neutrinos/antineutrinos estimated in Ruffert et al. (1996) take into account all four of those species. We also note that several quantities, including the chemical potentials, are obtained from EOS table interpolation.

2.3.2. Optical Depth

The transition between the two regimes will be set by the optical depth τ_{ν_i}, which is also needed to obtain the diffusion timescale. In order to get the optical depth, we consider the following reactions as the source of neutrino opacity:

$$\nu_e + n \rightarrow p \ + \ e^- \tag{48}$$

$$\bar{\nu}_e + p \rightarrow n \ + \ e^+ \tag{49}$$

$$\nu_i + p \rightarrow \nu_i + p \tag{50}$$

$$\nu_i + n \rightarrow \nu_i + n. \tag{51}$$

The opacities are obtained from Ruffert et al. (1996). Electron scattering is neglected.

The usual global approach to calculate the optical depth of a point in the flow would be to integrate the opacity over all directions and determine the path of minimal absorption. This approach assumes that the neutrino will follow a straight path. However, we follow Neilsen et al. (2014) and Siegel & Metzger (2018), where a local, iterative approach is used instead of a global calculation, and where crooked minimal paths are acceptable. The optical depth is calculated by obtaining the shortest path of the neutrino out of the star using its neighbors. For the first time step, we begin by initializing the optical depth grid to zero. Next, we perform the first iteration, where we estimate the optical depth at each cell as the minimum of the optical depth of its neighbor ($\tau_{\nu_i,\text{neighbor}}$) plus the optical depth needed for the neutrino to reach that neighbor ($\bar{\kappa}_{\nu_i}(g_{kj}dx^k dx^j)^{1/2}$):

$$\tau_{\nu_i} = \min\left(\tau_{\nu_i,\text{neighbor}} + \bar{\kappa}_{\nu_i}(g_{kj}dx^k dx^j)^{1/2}\right), \tag{52}$$

where $\tau_{\nu_i,\text{neighbor}}$ is the optical depth of the neighboring cell, $\bar{\kappa}_{\nu_i}$ is the average opacity between the cell and its neighbor, and $(g_{kj}dx^k dx^j)^{1/2}$ is the distance to the neighboring cell calculated by taking the average value of g_{kj} between the local and neighboring cells. We minimize over all neighbors.

This essentially traces the path of least resistance of the neutrino to a neighbor. We update the entire grid and perform the next iteration, where again, we minimize over all the adjacent neighbors. The next iteration will show the path to the neighbor two cells away. As we do more iterations, we trace the path of least resistance that the neutrinos will take out of the star. This will lead us to the final optical depth. During the first time step, we initialize the optical depth by by performing $20N_{\text{max}}$ iterations, where N_{max} is the maximum number of cells in each direction, independent of resolution. This is done to trace a path to the edge of the domain initially. After the initial calculation, which has a fixed number of iterations, we continue to do iterations to obtain the final optical depth; however, we impose a convergence criterion in order to minimize the number of iterations. In order to converge, we set conditions on the difference between iteration $k-1$ and k:

$$R_{\text{change},\tau}(k) \equiv \frac{|\sum\tau_{k-1} - \sum\tau_k|}{\sum\tau_{k-1}} < \epsilon_1 \tag{53}$$

or

$$\frac{|R_{\text{change},\tau}(k-1) - R_{\text{change},\tau}(k)|}{R_{\text{change},\tau}(k-1)} < \epsilon_2, \tag{54}$$

where $\sum\tau_k$ is the sum of all the optical depths in the grid at iteration k, and ϵ_1 and ϵ_2 are parameters that we choose to be $\epsilon_1 = 10^{-4}$ and $\epsilon_2 = 10^{-3}$, respectively. Only a few iterations are needed for convergence after the initial guess.

3. Validation Tests for the Tabulated EOS

In this section, we describe the tests performed to validate the implemented EOS tables.

3.1. Testing the Conserved to Primitive Variables Routine

In order to validate the routines that transform the conserved variables into primitive variables with tabulated EOS, we created primitive variables out of a grid of density and temperature values within the EOS table. The magnetic field was set randomly to be either aligned or antialigned with the velocity vector. The magnitude of the magnetic field was set to be such that $b^2/2 = \left(\frac{P_{\text{mag}}}{P_{\text{gas}}}\right)P_{\text{gas}}$, where $(P_{\text{mag}}/P_{\text{gas}})$ is set as a parameter, P_{mag} is the magnetic pressure, and P_{gas} is the gas pressure. We then obtained a set of conserved variables based on these primitives. The true primitives were then varied by randomly adding or subtracting a 5% perturbation to each primitive. This test is based on Siegel et al. (2018).

We then used these primitives as initial guesses for the various routines that transform the conserved variables to primitive variables and compared the resultant solution to the original.

We show the error we obtained for all primitive variables in Figure 1. It can be seen that the recovery error is low. Additionally, the figure shows that the 3D method is less robust, but more accurate, which is the reason it is set as the primary routine. The different 2D methods and the "Palenzuela" routine are more robust, but less accurate (and slower) than the 3D method, so they serve better as backup routines.

3.2. Torus in Hydrostatic Equilibrium

To test the EOS implementation, we simulated a nonmagnetized torus that is in hydrostatic equilibrium with no leakage scheme, following Fishbone & Moncrief (1976).

Figure 2 shows the 3D hydrodynamical evolution of a torus constructed to be in hydrostatic equilibrium with a tabulated EOS without neutrino cooling. There are perturbations, in particular near the BH, due to accretion onto the BH, but the density is low in those regions. As can be seen from the figure, the torus remains in hydrostatic equilibrium throughout the simulation.

3.2.1. Initial Conditions inside the Torus

The specific enthalpy inside the torus is implemented via Equation (3.6) of Fishbone & Moncrief (1976), but adding $\ln h_{\text{min}}$ to the integration constant (see Section 3.2.2). By construction, the torus is in hydrostatic equilibrium with the ambient atmosphere. We also set the torus to be isentropic and have uniform electron fraction. Given a specific entropy s_{disk}, a specific enthalpy given by Fishbone & Moncrief (1976), and an electron fraction $Y_{e,\text{disk}}$), the temperature and density of the disk
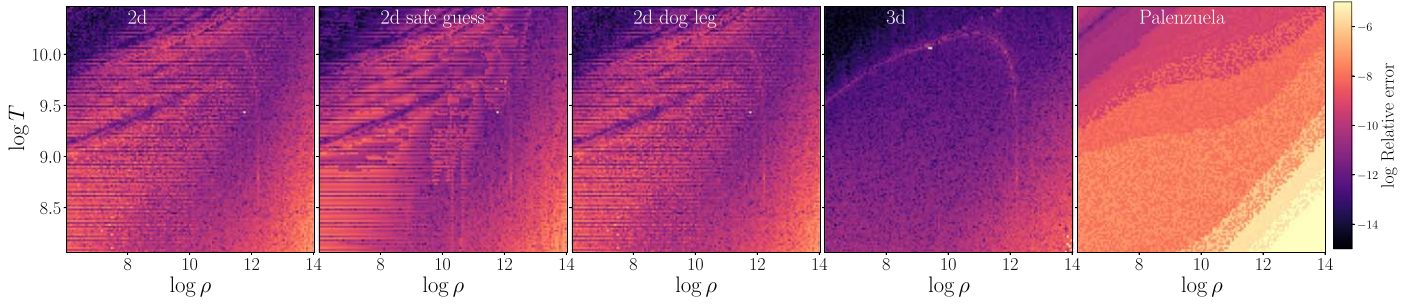
Figure 1. Relative error comparing primitive variables created from a grid of density and temperature after we performed the conversion from conserved variables to primitive variables. The primitive variables were created with $Y_e = 0.1$, the Lorentz factor $\gamma = 2$, $\log \frac{P_{\text{mag}}}{P_{\text{gas}}} = -5$, and a Minkowski metric. We perturbed them by 5% and then recovered them using our conserved to primitive routines. The error is calculated by summing over the relative error of each primitive variable compared to the original. We did this for 2^{14} points in the shown range. The 2D routines failed only once, the 3D routines failed 11 times, and the Palenzuela routine did not fail in this range. Density is in units of g cm^{-3}, and temperature is in units of Kelvin. Here, we compare different routines, described in the text.

are found by solving the following equations:

$$s_{\text{disk}} = s(\rho, T, Y_e) \tag{55}$$

$$h = h(\rho, T, Y_e), \tag{56}$$

where s is the specific entropy.

3.2.2. Atmosphere

In the classical torus, the boundaries of the torus are defined where $h = 1$. In the tabulated EOS, though, negative internal energy densities are allowed because the internal energy per nucleon is measured relative to the free neutron rest mass energy. In this case, the minimum specific enthalpy is not restricted to 1, but rather it can be $1 > h_{\text{min}} > 0$, where h_{min} is the specific enthalpy from the table, given the atmospheric density and the disk's electron fraction and specific entropy. Thus, we set the torus boundary to be where $h = h_{\text{min}}$. For the background atmosphere, we set the minimum atmospheric density ρ_{atm} as a parameter. We then find the minimum specific enthalpy by doing a table inversion and finding $h_{\text{min}} = h(\rho_{\text{atm}}, s_{\text{disk}}, Y_{e,\text{disk}})$. We also find the atmospheric temperature by doing a table inversion $T_{\text{atm}} = T(\rho_{\text{atm}}, s_{\text{disk}}, Y_{e,\text{disk}})$.

The density in the background is set to

$$\max\left(\rho_{\text{atm}}, \frac{\rho_0}{r^2}\right), \tag{57}$$

where we set ρ_0 as a parameter as well. The background atmosphere temperature is set to

$$\max\left(T_{\text{atm}}, \frac{T_0}{r}\right), \tag{58}$$

where T_0 is a parameter. The power-law dependence is set to provide the background atmosphere with more pressure support so that it does not rapidly accrete onto the BH. This ultimately helps with robustness near the BH, as the low-density and low-temperature zones with high velocity are where the conserved to primitive routines tend to fail. We note that, in the region where there is a power-law dependence, the specific enthalpy is not a constant, whereas once the background atmosphere is set to be constant, everything is thermodynamically consistent because it was constructed with the tabulated EOS tables. We set the electron fraction of the atmosphere to a constant value found by assuming β-equilibrium (where the neutrino chemical potential is zero) at T_{atm} and ρ_{atm}.

The units are normalized so that the maximum density in the torus is set to $\rho_{\text{max}} = 1$ in code units, which in this case corresponds to $\rho_{\text{max}} = 5.4 \times 10^8$ g cm^{-3} in cgs units. In the simulation we performed, the torus has a constant electron fraction of $Y_e = 0.1$ and a specific entropy of $10k_{\text{B}}$/baryon, where K_{B} is Boltzmann's constant. The background atmosphere is characterized by $\rho_{\text{atm}} = 6000$ g cm^{-3}, $\rho_0 = 3 \times 10^5$ g cm^{-3}, and $T_0 = 0.4$ MeV. We used the SLy4 table with NSE from Schneider et al. (2017), and with that table the minimum specific enthalpy for our parameters is set to $h_{\text{min}} = 0.9974$ (in code units), and $T_{\text{atm}} = 0.0053$ MeV. The electron fraction in the atmosphere, given by β-equilibrium, is set to $Y_{e,\text{atm}} = 0.45$. The boundary conditions are outflow in the outer radial boundary, reflective in the angular coordinate θ, and periodic in the angular coordinate ϕ. The metric is Kerr–Schild in spherical coordinates for a non-spinning BH.

4. Validation Tests for the Leakage Scheme

In this subsection, we describe how we tested the leakage scheme in the optically thin regime and for finite optical depth.

4.1. Testing the Optically Thin Regime

Following Miller et al. (2019a), we tested the leakage scheme in an optically thin regime by considering an isotropic gas of constant density and temperature such that the gas is optically thin to neutrinos. We conducted separate tests of both reactions in the charged β-process, wherein we included only either the neutrinos or the antineutrinos.

In this case, the GRMHD equations reduce to

$$\partial_t T^t{}_t = \mathcal{Q}., \tag{59}$$

$$\partial_t Y_e = \mathcal{R}/\rho, \tag{60}$$

where $\mathcal{R}$ and $\mathcal{Q}$ are the respective emission/absorption and energy-loss rates due to neutrinos or antineutrinos of the reactions in the β-process. The rates need to be calculated semi-analytically, since they depend on interpolated quantities, such as the degeneracy parameters. We can then solve the equations semi-analytically with a set of initial conditions and compare to simulations. We chose the initial density and temperature such that the medium is optically thin to neutrinos and antineutrinos.

For the initial conditions, we used an initial density of 617714 g cm^{-3} and temperature of 1 MeV, chosen so that the medium is optically thin to neutrinos and antineutrinos. We used $Y_{e,0} = 0.5$ and $Y_{e,0} = 0.005$ for the electron neutrino and
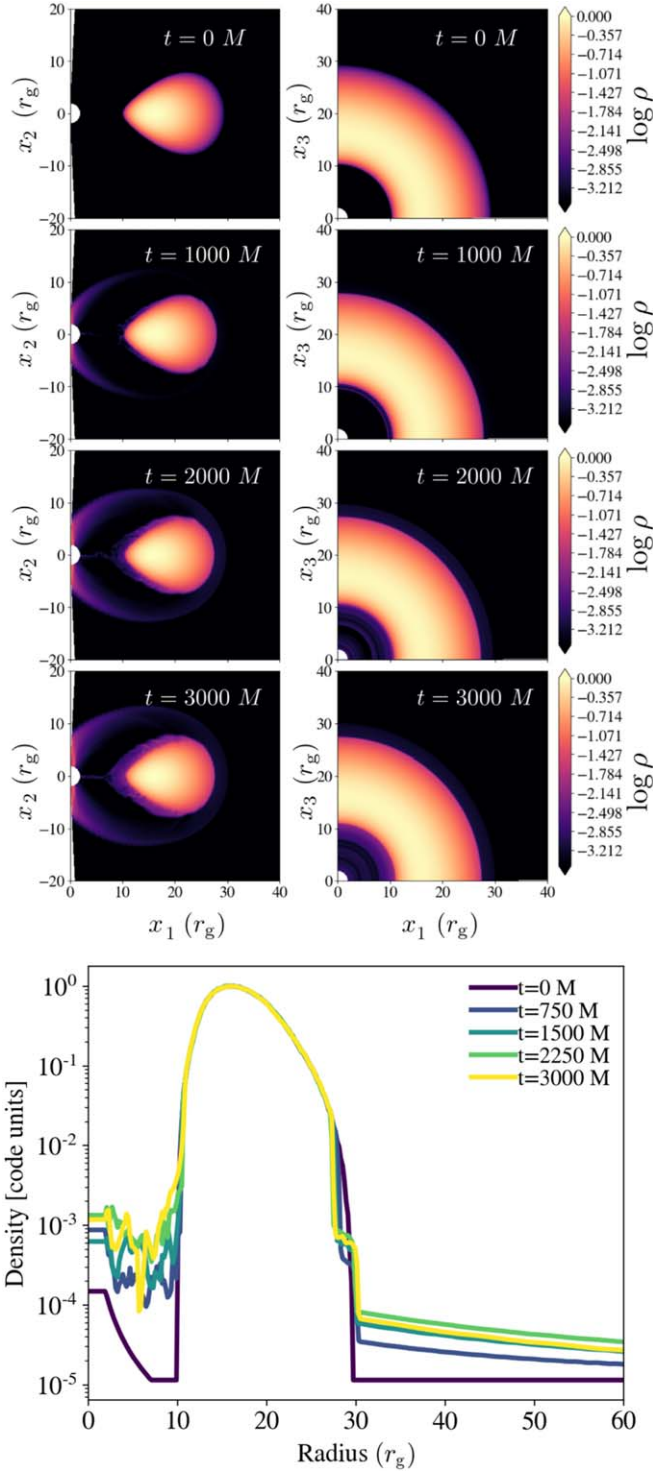
Figure 2. Top panel: evolution of a torus in hydrostatic equilibrium with a tabulated EOS and no neutrino-leakage scheme. We show the meridional (left) and equatorial (right) cut. The initial conditions are set as described in Section 3.2. Here, x_1, x_2, and x_3 correspond to the coordinates x, z, and y, respectively. Bottom panel: density as a function of radius for different times in the equator.

antineutrino tests, respectively. We used $2 \times 2 \times 1$ cells in each direction using a Cartesian grid with Minkowski metric.

In Figure 3, we show the comparison between the semi-analytical solution and the simulation for the β-process both for neutrinos and antineutrinos. We compare the change in the electron fraction due to the absorption/emission rate and the
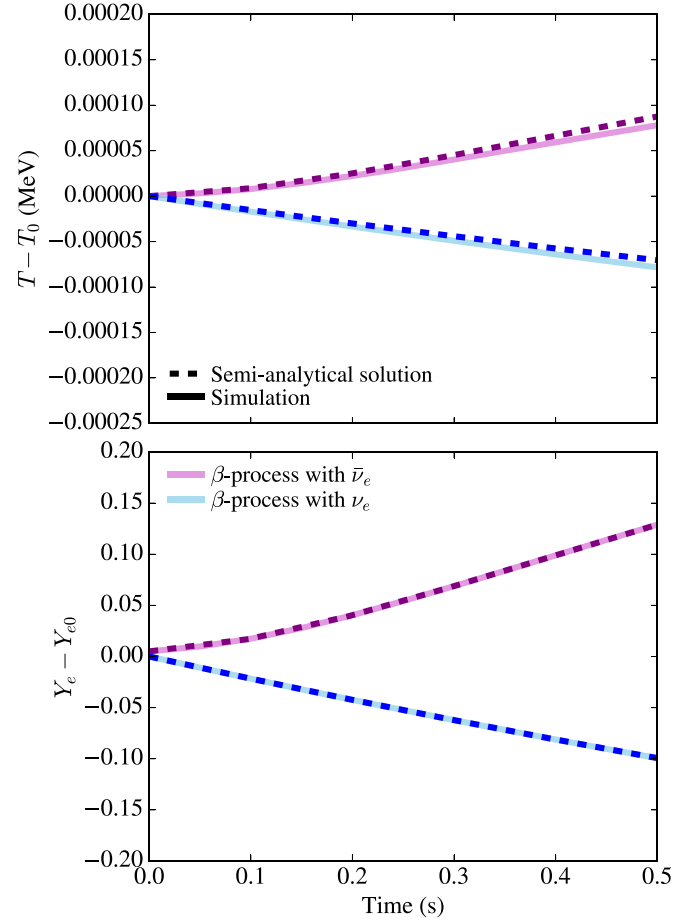
Figure 3. Comparison of the semi-analytical solution (dotted line) with the simulation (solid line) for the evolution of the temperature and electron fraction of an isotropic, optically thin gas with constant density.

change in temperature due to the heating/cooling rate. As can be seen from the figure, HARM3D+NUC is able to recreate the semi-analytical solution.

4.2. Testing the Optically Thick Regime

4.2.1. Constant Density Circular Disk

In order to test the optical depth calculation, we simulated a circular disk with uniform density and temperature embedded in an optically thin medium of constant density and temperature. The advantage of this scenario is that we can calculate the opacity inside the circle and then calculate the optical depth analytically. This way, we can compare to the simulation. The simulations were performed in 2D, and the domain is $2r_g$, where $r_g = GM/c^2$ is the gravitational radius. We used a Minkowski metric with spherical coordinates. There are outflow conditions on the radial boundaries. The optical depth in the outer radial boundary was set to zero so that the neutrinos and antineutrinos could escape the domain. We simulated an optically thick circular disk that has a constant density of $9.8 \times 10^{13}\,\mathrm{g\,cm^{-3}}$, an electron fraction of 0.1, and a temperature of 8 MeV, embedded in an optically thin medium, with a density of $6 \times 10^7\,\mathrm{g\,cm^{-3}}$, an electron fraction of 0.5, and a temperature of 0.01 MeV. Figure 4 shows the optical depth for both the electron neutrino and antineutrino for different resolutions. As can be seen from the figure, the initial guess for the optical depth is accurate and the convergence to the
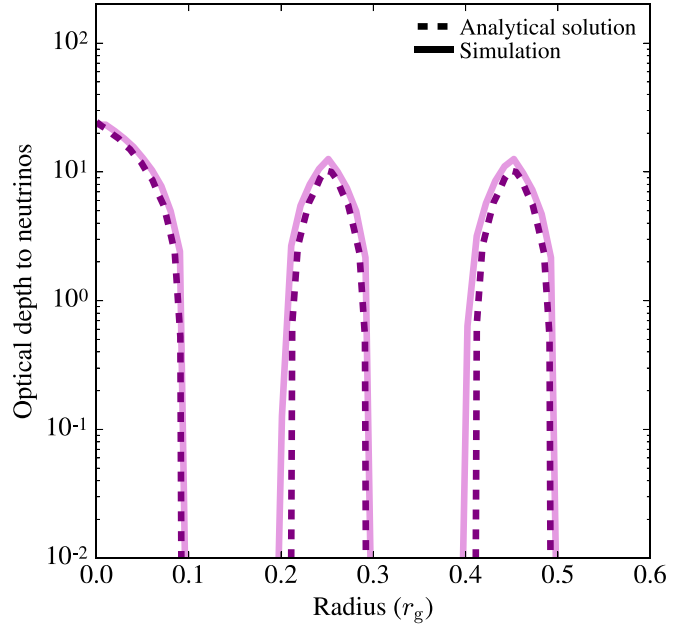
Figure 5. Comparison of the analytical solution (dotted line) of the optical depth to neutrinos with simulations (solid line).

domain. We simulated three stripes of material with high optical depth: $\rho = 9.8 \times 10^{13}\,\mathrm{g\,cm^{-3}}$, $Y_e = 0.1$, and $T = 8\,\mathrm{MeV}$. In between the stripes, the optically thin gas was initialized to $\rho = 6 \times 10^7\,\mathrm{g\,cm^{-3}}$, $Y_e = 0.5$, and $T = 0.01\,\mathrm{MeV}$. The high-opacity stripes start at $r = 0r_\mathrm{g}$ and have a width of $r = 0.1r_\mathrm{g}$. The next stripes are located in $r = 0.2r_\mathrm{g}$ and $r = 0.4r_\mathrm{g}$.

We show the results from this setup in Figure 5, where we compare the results from the simulation with the analytical estimate (length units are in r_g):

$$\tau_{\mathrm{analytical}} = \begin{cases} \int_0^{0.2} \kappa dr & r \leqslant 0.2 \\ \int_{0.2}^{0.25} \kappa dr & 0.2 \leqslant r \leqslant 0.25 \\ \int_{0.25}^{0.35} \kappa dr & 0.25 \leqslant r \leqslant 0.35. \\ \int_{0.4}^{0.45} \kappa dr & 0.4 \leqslant r \leqslant 0.45 \\ \int_{0.45}^{0.55} \kappa dr & 0.45 \leqslant r \leqslant 0.55 \end{cases} \qquad (61)$$

5. Magnetized Disk

In this section, we apply our new code HARM3D+NUC to a magnetized torus in 3D that approximates a post-merger disk. We use both the tabulated EOS and the leakage scheme in this test.

5.1. Initial Conditions

The initial conditions inside the torus follow a setup similar to that of Section 3.2.1, but with the addition of a poloidal magnetic field. In order to start with a magnetic field devoid of magnetic monopoles, we first set the vector potential to a prescribed distribution and calculate its curl using a finite difference operator compatible with our constrained transport method (see Zilhão & Noble 2014 for further details). Our poloidal magnetic field distribution results from a vector

Figure 4. Comparison of the analytical solution (dotted line) of the optical depth with simulations (solid line) for different resolutions. The labels indicate the number of cells in each direction. The top panel is the antineutrino optical depth, and the Bottom panel is the neutrino optical depth.

solution does not change with resolution. At smaller optical depths, the optical depth is slightly overestimated at lower resolutions, but as the optical depth increases, the solution does not depend noticeably on resolution.

4.2.2. Stripes

We can also test the optical depth algorithm by simulating stripes of high-density material with low-density material in between. In this scenario, it is expected that a neutrino created in the region with high optical depth material will travel to the region with low optical depth and stream freely from the surface. For the simulation, we used $4096 \times 96 \times 1$ cells. The simulations were performed in 2D, and the domain is $1r_\mathrm{g}$ large in radial extent, where $r_\mathrm{g} = GM/c^2$ is the gravitational radius. We used a Minkowski metric with spherical coordinates and outflow conditions at the radial boundaries. The optical depth at the outer radial boundary was set to zero so that the neutrinos and antineutrinos could escape the

Table 1
Parameters Used in the Simulation

Parameter	Value
Disk radius of maximum pressure	$9r_{\rm g}$
Disk inner radius	$4r_{\rm g}$
Mass of disk	$0.03M_{\odot}$
Y_e in the disk	0.1
Specific entropy in the disk	7 $k_{\rm b}$/baryon
$(P_{\rm gas}/P_{\rm mag})$	100
BH spin	0.9375
BH mass	$3M_{\odot}$
Specific enthalpy at boundary	0.9977 [code units]
Temperature at radius of maximum pressure	4.4 MeV

potential with only one nonzero component,

$$A_{\phi} = \max{(\overline{\rho}/\rho_{\rm max} - \rho_{0,\rm mag}, 0)}, \qquad (62)$$

where $\overline{\rho}$ is the average density at that position and $\rho_{\rm max} = 1.66 \times 10^{11} \rm\, g\, cm^{-3}$ is the maximum density of the torus. We set $\rho_{0,\rm mag} = 0.2$ in code units, which corresponds to $\rho_{0,\rm mag} = 3.33 \times 10^{10} \rm\, g\, cm^{-3}$. We then build the magnetic field with the vector potential and normalize its magnitude such that the ratio of the integrated gas pressure to integrated magnetic pressure is 100. Inside the disk, the matter is set to be neutron-rich, $Y_e = 0.1$. The treatment of the atmosphere is the same as in Section 3.2.2, except the density scales as $r^{-3/2}$. In the atmosphere, the electron fraction is set to its value in β-equilibrium, where the chemical potential of the neutrinos is set to zero. We show the parameters used in Table 1.

The simulations were performed in 3D on a grid designed to focus more cells about the equator and toward the black hole horizon. We use the same grid as defined in Noble et al. (2010) but with different parameters. The azimuthal grid spacing is uniform. The logarithmic radial grid is such that $\Delta r/r$ is fixed and the ith cell center is located at:

$$r_i = r_{\rm min} \exp{[(i + 1/2) \log_{10}(r_{\rm max}/r_{\rm min})/N_r]}, \qquad (63)$$

with $r_{\rm min} = 1.303r_{\rm g}$, $r_{\rm max} = 2000r_{\rm g}$, and $i \in [0, N_r - 1]$. The θ grid uses a high-order polynomial function to provide a nearly uniform grid spacing spacing near the equator:

$$\theta_j = \frac{\pi}{2}\left[1 + (1 - \xi)(2x_j^{(2)} - 1) + \left(\xi - \frac{2\theta_c}{\pi}\right)(2x_j^{(2)} - 1)^n \right], \qquad (64)$$

where ξ is a parameter controlling the severity of the focusing, n is the order of polynomial used in the transformation, θ_c is the opening angle of the polar regions we excise, $x_j^{(2)} \equiv (j + 1/2)/N_{\theta}$, and $j \in [0, N_{\theta} - 1]$. In our run, we used $\theta_c = \pi 10^{-14}$, $\xi = 0.65$, and $n = 7$. The number of cells per dimension used was $N_r \times N_{\theta} \times N_{\phi} = 1024 \times 160 \times 256$.

5.2. Scaling Tests

We performed scaling tests for this run for three different numbers of processors: 5120, 2560, and 1280 processors. For this setup, the numbers of time steps in the code per second per processor were 0.000723, 0.000781, and 0.000868, respectively. The difference between 5120 and 1280 processors is around 17%. If we exclude the neutrino-leakage scheme and
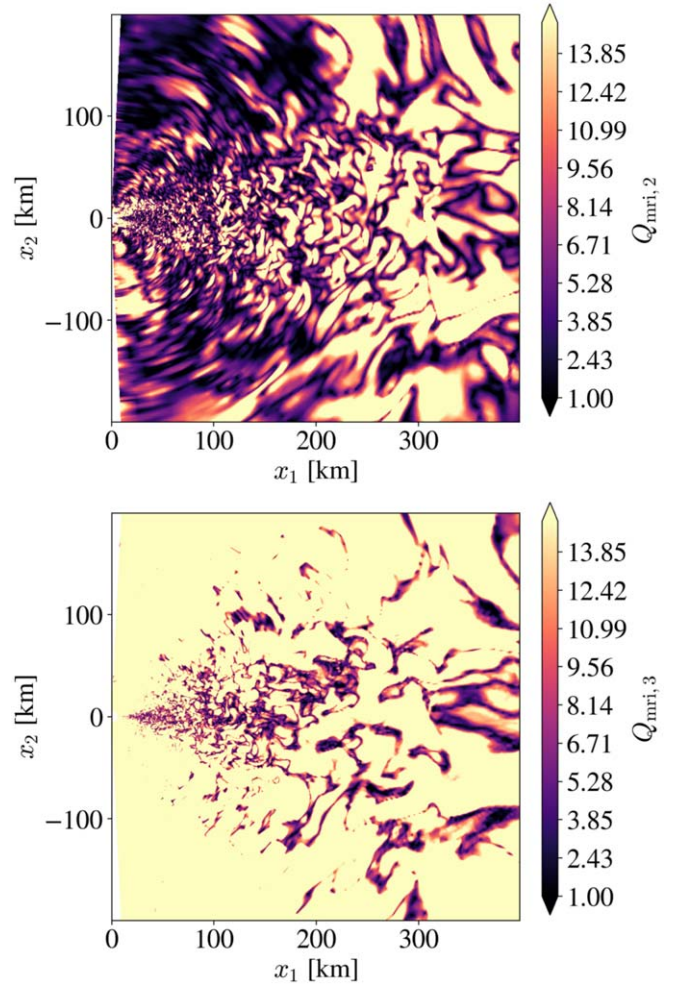
Figure 6. Shown is a meridional cut of the MRI quality factors $Q_{\rm mri,2}$ and $Q_{\rm mri,3}$ at 114 ms, where the subscripts for $Q_{\rm mri,2}$ and $Q_{\rm mri,3}$ correspond to the coordinates θ and ϕ, respectively.

include only a tabulated EOS, for 2560 processors, the number of steps per second per processor is 0.001328, which makes the leakage 58% slower than only considering the tabulated EOS.

5.3. Magnetic Turbulence

In order to confirm that we are adequately resolving magnetic turbulence, we display in Figure 6 the number of grid cells per wavelength of the fastest growing mode of the magnetorotational instability (MRI), defined as (Noble et al. 2010; Hawley et al. 2011, 2013; Sorathia et al. 2012)

$$Q_{\rm mri,x} = \frac{\lambda_{x,\rm mri}}{\Delta_x}, \qquad (65)$$

where $x = \theta, \phi$, Δ_x is the cell size, and the wavelength of the fastest MRI growing mode is

$$\lambda_{x,\rm mri} = \frac{2\pi}{\Omega}\frac{|b^x|}{\sqrt{\rho h + b^2}}. \qquad (66)$$

As can be seen in Figure 7, our grid satisfies the criterion of Sano et al. (2004) everywhere except for later times within $r < 50$ km. While our results fail to meet criteria for asymptotic MRI convergence set forth in Hawley et al. (2011), our disk does satisfy $Q_{\rm mri,3} > 10$ everywhere, and $Q_{\rm mri,2} > 6$ for

Figure 8. Density of a magnetized torus, including the impact of neutrinos at 114 ms. Shown are an equatorial cut (top panel) and a meridional cut (bottom panel).
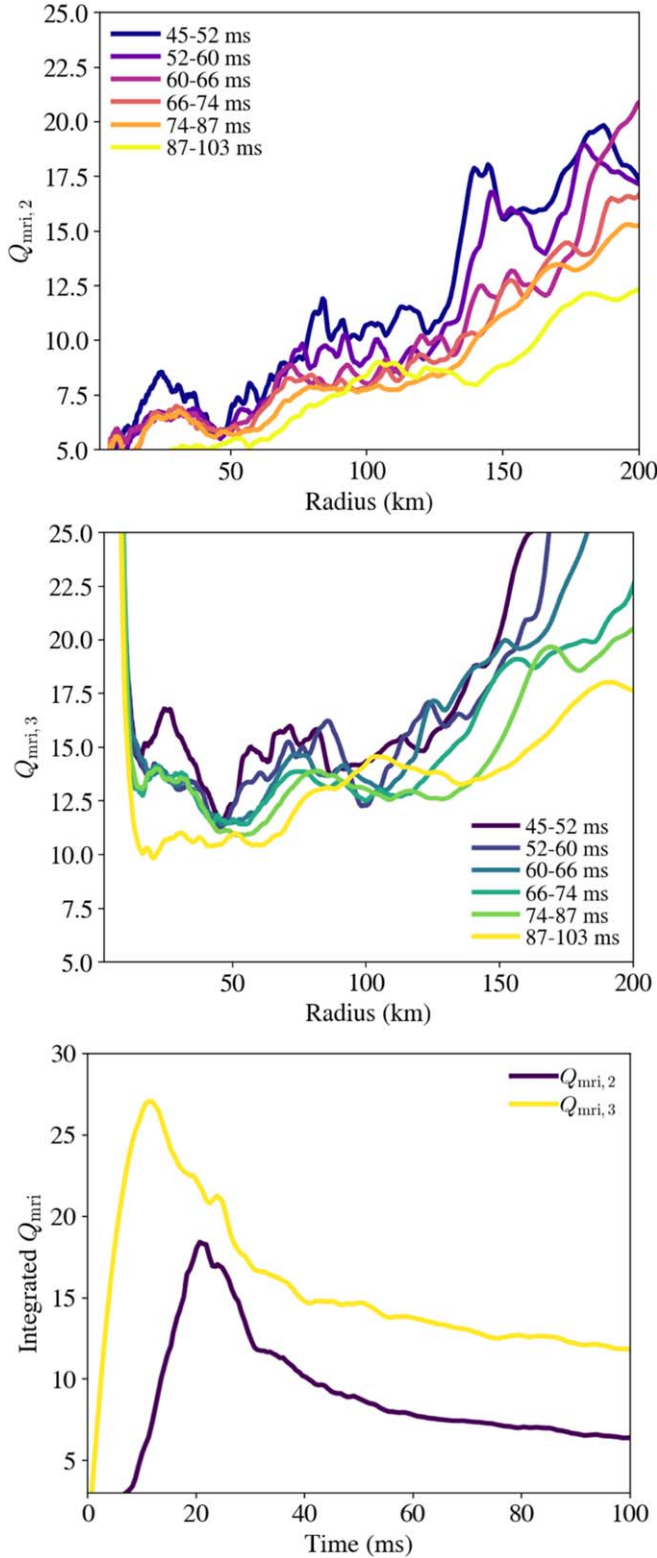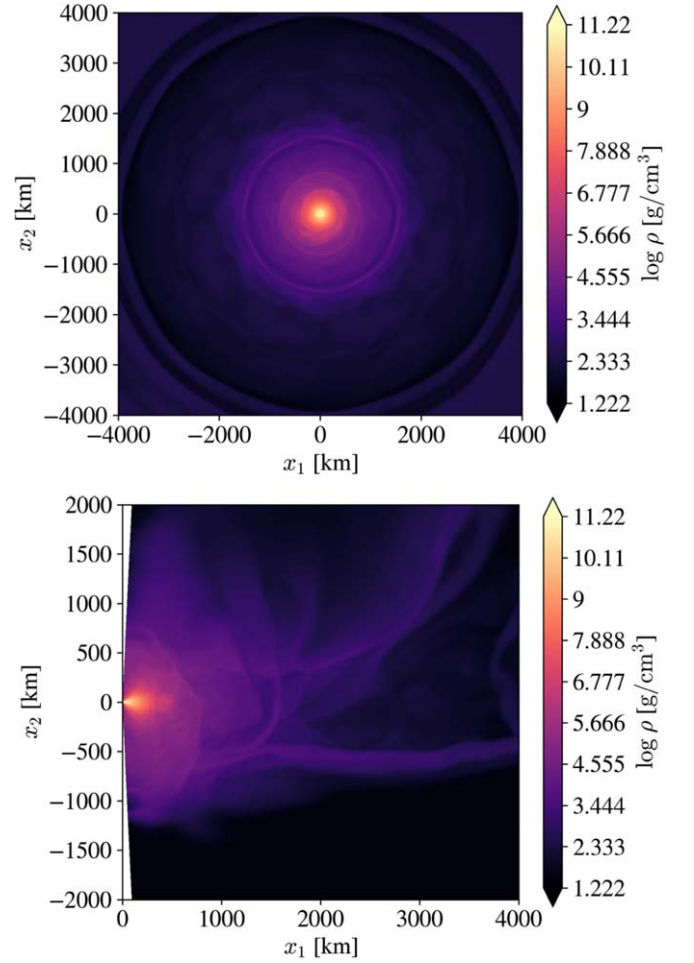

Figure 7. Top and middle panel: shell-integrated mass-weighted quality factors as a function of radius, averaged over different epochs of time. Bottom panel: mass-weighted quality factors integrated over angles and radii that are less than 150 km: $\int_{0\,\mathrm{km}}^{150\,\mathrm{km}} \int\int Q_{\mathrm{mri}} \rho \sqrt{-g}\, drd\phi d\theta \Big/ \int_{0\,\mathrm{km}}^{150\,\mathrm{km}} \int\int \sqrt{-g}\, \rho drd\phi d\theta$.

$r \gtrsim 50$ km for most of the run. One reason why our simulation may not reach larger Q_{mri} values is because we used the same random perturbations across all MPI processes in the initial conditions. Because we used 16 subdomains in the azimuthal

dimension, this means that the simulation is nearly periodic over $\Delta\phi = \pi/8$, and the azimuthal modes with $m < 8$ start off significantly weaker because they are seeded with perturbations at only the round-off error level.

5.4. Impact of Neutrinos and EOS

Magnetic stresses will transport angular momentum in the disk, heating the gas, which will produce a high-velocity outflow (Fernández & Metzger 2013a; Siegel & Metzger 2018). This outflow will be affected by the addition of neutrinos formed through weak reactions. In the midplane, neutrinos will carry significant amounts of energy, which will cool and make the disk geometrically thinner. Another outflow is also expected to occur in the outer regions of the disk, due to the release in nuclear binding energy when there is recombination of free nucleons into α-particles, which produces enthalpy and unbinds material (Lee et al. 2009; Fernández & Metzger 2013a). In this subsection, we show the impact of both the emission of neutrinos and the recombination of free nucleons.

In Figures 8 and 11, we display the outflows that result from our simulations of a neutrino-cooled magnetized disk at 114 ms. In Figures 9 and 10, we plot the electron fraction and the density, respectively, at $t = 114$ ms. Movies can be found here.[24]

---

[24] https://www.youtube.com/playlist?list=PLurnnzvqZvZaqLWlT2BVm POlDm5P3BUOz
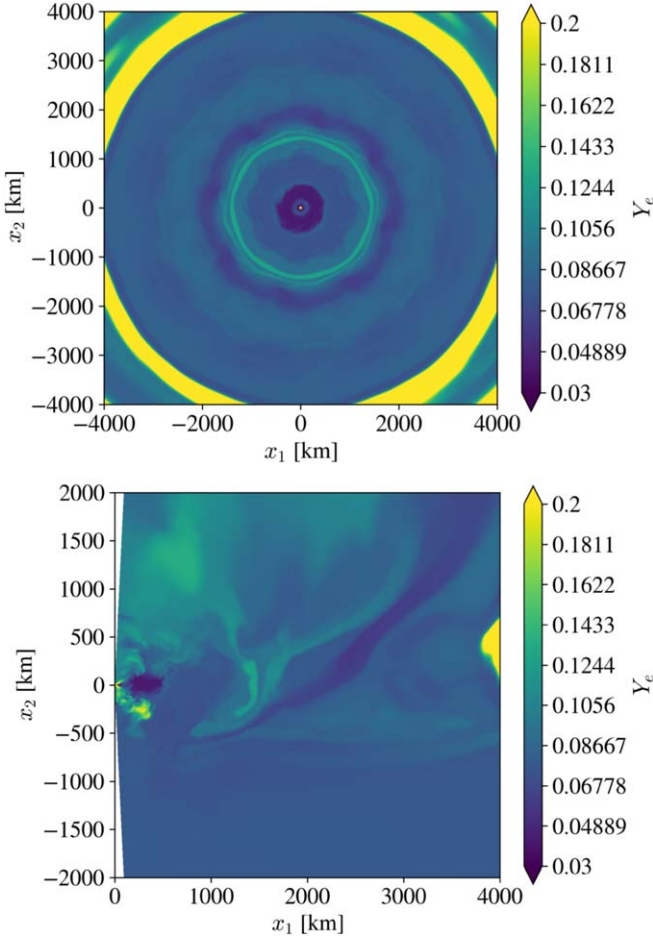
Figure 9. Electron fraction of a magnetized torus, including the impact of neutrinos at 114 ms. Shown are an equatorial cut (top panel) and a meridional cut (bottom panel).
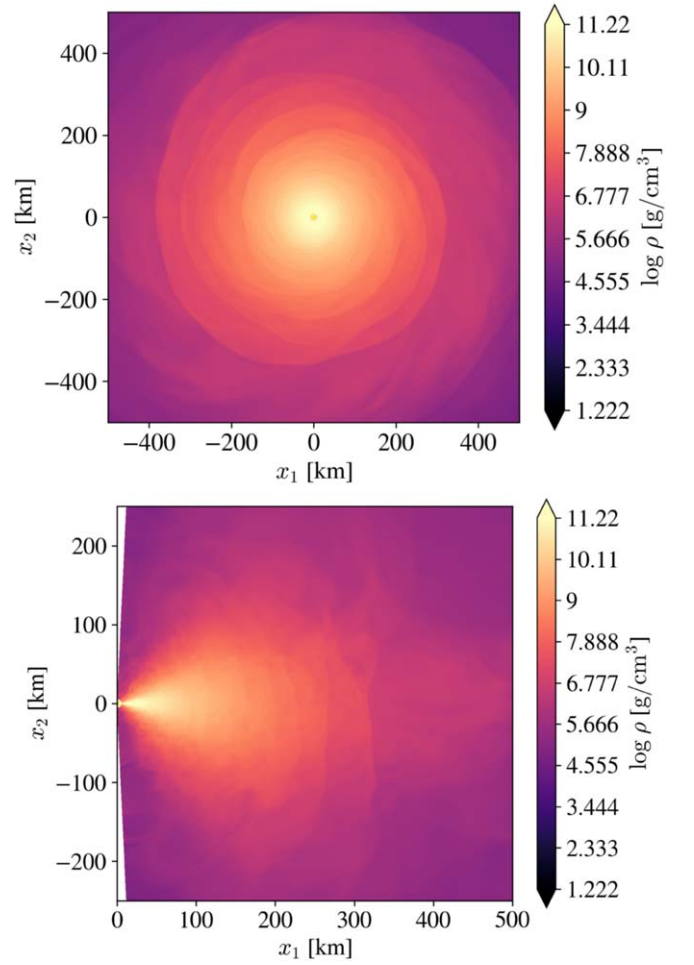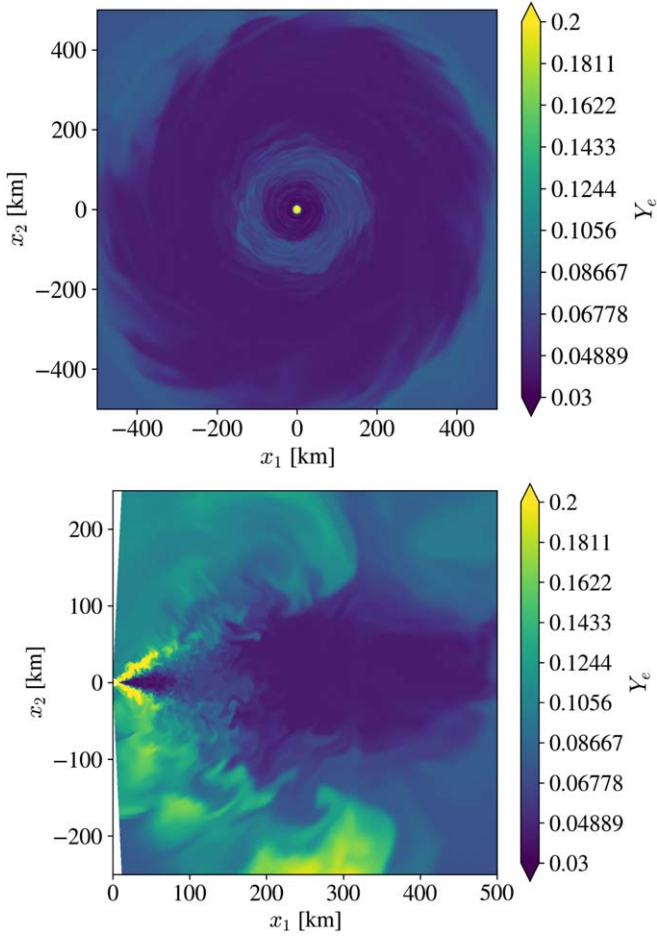

Figure 10. Zoomed-in version of the density of a magnetized torus, including the impact of neutrinos at 114 ms. Shown are an equatorial cut (top panel) and a meridional cut (bottom panel).

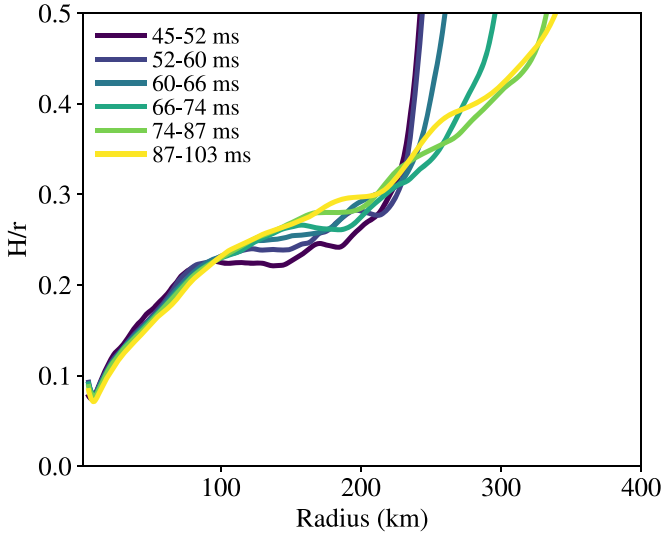Neutrino cooling is expected to happen on the diffusion timescale, which is on the order of milliseconds—much shorter than our evolution timescale. The inner regions of the disk are very neutron-rich, confirming the self-regulating phase found in Siegel & Metzger (2017, 2018). In this phase, there is a balance between the neutrino cooling and the heating driven by MHD that self-regulates the electron degeneracy parameter, and the final state is a neutron-rich disk (Siegel & Metzger 2017, 2018). We note that, although this new code does not include neutrino absorption in the ejecta, absorption will modify the electron fraction in the outflow (Just et al. 2021).

In Figure 12, we plot the geometrical thickness of the disk, or H/r. We estimated this thickness using the scale height H following Noble et al. (2012),

$$H = \frac{\langle \rho \sqrt{g_{\theta\theta}} |\theta - \pi/2| \rangle}{\langle \rho \rangle}, \qquad (67)$$

where $\langle X \rangle$ is the average of the quantity X over a spherical shell,

$$\langle X \rangle = \frac{\int X \sqrt{-g}\, d\theta d\phi}{\int \sqrt{-g}\, d\theta d\phi}. \qquad (68)$$

In the top panel of Figure 13, we show the mass accretion rate through the innermost stable circular orbit as a function of time, and in the bottom panel, we show the accretion rate as a function of radius. The outflow can be clearly seen as a negative mass accretion rate at larger radii, as well as a settling of the mass accretion rate as time passes.

In the deepest regions of the disk, the heating due to MHD turbulence helps create neutrinos/antineutrinos, which escape, remove energy, and geometrically thin the disk. Recombination of free nucleons into α-particles releases binding energy, effectively increasing the enthalpy and unbinds material. The effect of recombination is less severe than the geometric thinning due to neutrino/antineutrino losses. This transition can be seen at around 150 km.

We may obtain the amount of energy radiated by each species of neutrino and antineutrino as was done in Siegel & Metzger (2018):

$$L_{\nu_i} = \int \alpha \gamma \mathcal{Q}_{\nu_i}^{\text{eff}} \sqrt{-g}\, d^3x. \qquad (69)$$

In Figure 14, we show the luminosity for each species. It can be seen that the electron neutrino (and antineutrino) dominate the emission over all of the other species of neutrino. The luminosity roughly follows the mass accretion rate as seen in Figure 13, as heating from the magnetic stresses ignites the creation of neutrinos/antineutrinos. This suggests the radiative

Figure 11. Zoomed-in version of the electron fraction of a magnetized torus, including the impact of neutrinos at 114 ms. Shown are an equatorial cut (top panel) and a meridional cut (bottom panel).
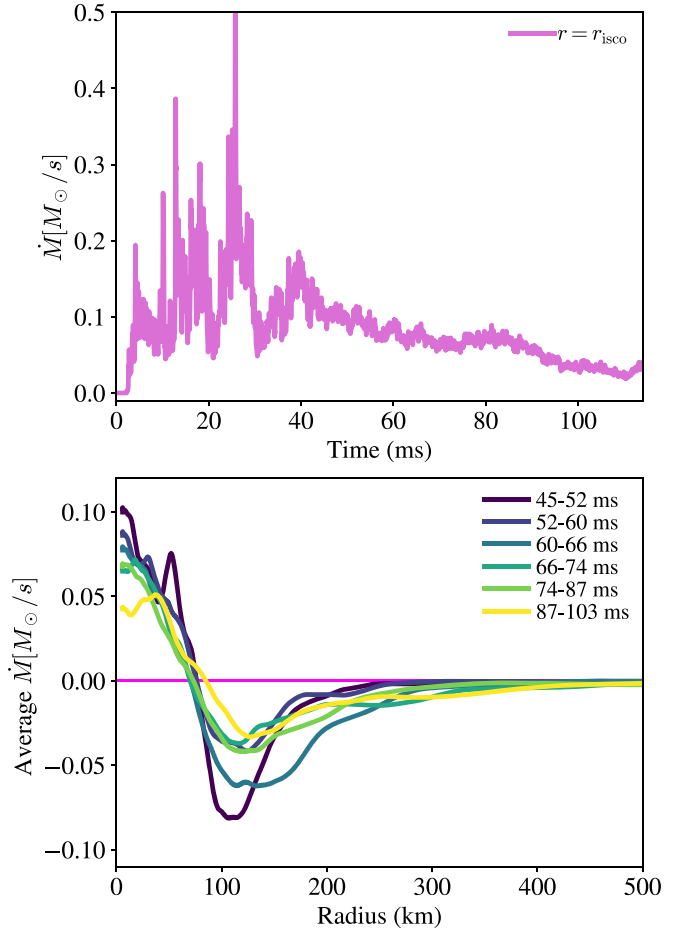

Figure 13. Top panel: mass accretion rate onto the innermost stable circular orbit (ISCO) of the BH as a function of time. Bottom panel: average mass accretion rate as a function of radius. We averaged the mass accretion rate between the times indicated in the legend.
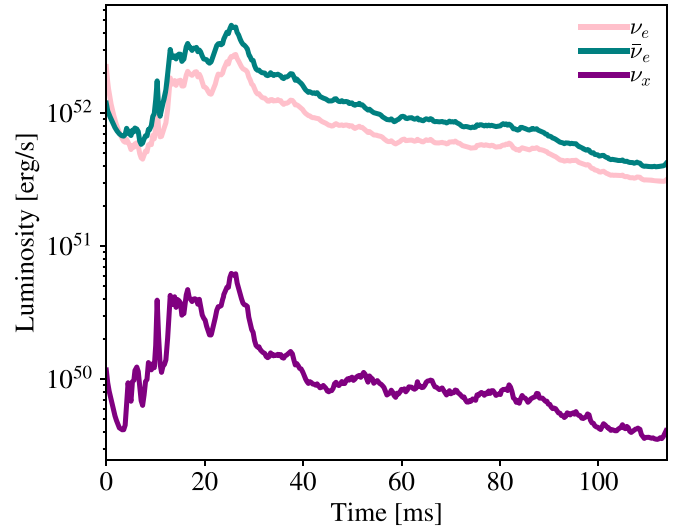

Figure 12. Shown is the geometrical thickness (H/r) of the disk, as a function of radius. The thickness is averaged between the indicated time in the legend.

Figure 14. Luminosity due to the different neutrino species as a function of time.

efficiency of neutrino/antineutrinos emission remains relatively steady.

Our initial conditions are similar (although not identical) to the initial conditions in Siegel & Metzger (2018). They

performed 3D simulations of a post-merger accretion disk with a relatively higher specific entropy and lower spin than this simulation. They used Cartesian coordinates, a Helmholtz EOS for relatively low densities, and a neutrino-leakage scheme.

They also evolved the disk for longer times (380 ms). Even though we use a different EOS (Sly4), the disk thickness is qualitatively similar. At the inner regions of the disk, neutrino cooling dominates, whereas at outer regions (at radius higher than around 100 km), recombination is responsible for making the disk geometrically thicker. The neutrino/antineutrino luminosities are comparable; Siegel & Metzger (2018) report a higher luminosity, but that could be attributed to the difference in the initial disk specific entropy.

As the outflow expands, it will cool and heavy elements will be created via the *r*-process. We will explore this nucleosynthesis in a future paper.

6. Summary

GRMHD simulations of post-merger accretion disks have advanced over the last few years, with better treatment of neutrinos and a more realistic EOS. In this paper, we present the addition of a neutrino-leakage scheme and a tabulated EOS into the computationally efficient, versatile GRMHD code HARM3D. This new addition to HARM3D, called HARM3D+NUC, has the potential to be used in a range of simulations where neutrinos are present. In this paper, we use the new code HARM3D+NUC to simulate an accretion disk resembling the post-merger phase of a binary neutron star, though other applications include collapsars (e.g., Siegel et al. 2019; Miller et al. 2020).

This paper shows how we implemented the tabulated EOS in the conserved variable to primitive variable routines, as well as the different methods we implemented and tested for performing this inversion. We show that using the 3D primary recovery method is the most accurate and efficient but least robust choice, which is why we also employ several 2D and 1D backup routines. The leakage scheme is implemented by adding the neutrino/antineutrino heating/cooling and emission/absorption terms as source terms in the equations of motion. We describe in detail an approach to obtain the optical depth locally and how we can use a convergence criterion to get the optical depth after a few iterations once the initial guess is made.

We show several tests for our new code. The tabulated EOS is tested by determining the relative error between original primitive variables and the recovered primitive variables. We also test the EOS by performing a simulation of a torus in hydrostatic equilibrium, showing that it stays in hydrostatic equilibrium throughout the entire simulation. We test the neutrino-leakage scheme in the optically thin regime by investigating the β-process in a constant-density gas. We test the optical depth algorithm in a constant-density circular disk and a stripes setup.

With our new tools, we simulate a magnetized high-density torus, which serves as an approximation to the accretion flow after the merger of two neutron stars. Magnetic stresses transport angular momentum from the disk, driving a high-velocity outflow. The outflow is affected by both the addition of neutrinos and the nuclear binding energy released from the recombination of nucleons to α-particles, which acts to geometrically thicken the disk. Neutrinos will alter the electron fraction of the ejecta, especially in the inner regions of the disk, whereas the recombination of nucleons is more prominent in the outer regions of the disk. This highlights the importance of modeling the accretion disk including neutrinos and an EOS that considers this extra unbinding of material due to recombination.

We plan to use the new code to do long-term evolutions of binary neutron star mergers starting from before the neutron stars merge to the evolution of the outflow. Heavy elements should be created via the *r*-process in this outflow as it expands and cools. We plan to use different codes and methods to treat the initial data, pre-merger/merger, and post-merger phases. The initial data for the neutron stars will be constructed using a modified version of LORENE (Gourgoulhon et al. 2016) we have developed. Binaries will be evolved until they merge and eventually form a black hole surrounded by an accretion disk using two GRMHD codes: IllinoisGRMHD (Etienne et al. 2015) and Spritz (Cipolletta et al. 2020). After the remnant has collapsed to a BH and the numerical metric has stabilized, we will interpolate the MHD primitives and numerical metric into the grid of HARM3D+NUC (F. G. Lopez Armengol et al. 2021, in preparation). After doing the appropriate tensorial transformations from the Cartesian base to the coordinate base of HARM3D+NUC, we will continue the post-merger evolution with HARM3D+NUC.

ORCID iDs

Ariadna Murguia-Berthier https://orcid.org/0000-0003-2333-6116
Scott C. Noble https://orcid.org/0000-0003-3547-8306
Enrico Ramirez-Ruiz https://orcid.org/0000-0003-2558-3102
Manuela Campanelli https://orcid.org/0000-0002-8659-6591
Riccardo Ciolfi https://orcid.org/0000-0003-3140-8933
Bruno Giacomazzo https://orcid.org/0000-0002-6947-4023
Bernard J. Kelly https://orcid.org/0000-0002-3326-4454
Julian H. Krolik https://orcid.org/0000-0002-2995-7717
Federico G. Lopez Armengol https://orcid.org/0000-0002-4882-5672
Ben Margalit https://orcid.org/0000-0001-8405-2649
Richard O'Shaughnessy https://orcid.org/0000-0001-5832-8517
Yosef Zlochower https://orcid.org/0000-0002-7541-6612

References

Abbott, B. P., Abbott, R., Abbott, T. D., et al. 2017a, PhRvL, 119, 161101
Abbott, B. P., Abbott, R., Abbott, T. D., et al. 2017b, ApJL, 848, L12
Baiotti, L., Giacomazzo, B., & Rezzolla, L. 2008, PhRvD, 78, 084033

Balbus, S. A., & Hawley, J. F. 1998, RvMP, 70, 1
Barnes, J., & Kasen, D. 2013, ApJ, 775, 18
Barnes, J., Kasen, D., Wu, M.-R., & Martínez-Pinedo, G. 2016, ApJ, 829, 110
Cerdá-Durán, P., Font, J. A., Antón, L., & Müller, E. 2008, A&A, 492, 937
Chen, W.-X., & Beloborodov, A. M. 2007, ApJ, 657, 383
Chevalier, R. A. 1989, ApJ, 346, 847
Ciolfi, R., Kastaun, W., Giacomazzo, B., et al. 2017, PhRvD, 95, 063016
Cipolletta, F., Kalinani, J. V., Giacomazzo, B., & Ciolfi, R. 2020, CQGra, 37, 135010
Coulter, D. A., Foley, R. J., Kilpatrick, C. D., et al. 2017, Sci, 358, 1556
Cowperthwaite, P. S., Berger, E., Villar, V. A., et al. 2017, ApJL, 848, L17
De, S., & Siegel, D. 2020, arXiv:2011.07176
Dessart, L., Ott, C. D., Burrows, A., Rosswog, S., & Livne, E. 2009, ApJ, 690, 1681
Di Matteo, T., Perna, R., & Narayan, R. 2002, ApJ, 579, 706
Dionysopoulou, K., Alic, D., & Rezzolla, L. 2015, PhRvD, 92, 084064
Drout, M. R., Piro, A. L., Shappee, B. J., et al. 2017, Sci, 358, 1570
Eichler, D., Livio, M., Piran, T., & Schramm, D. N. 1989, Natur, 340, 126
Etienne, Z. B., Paschalidis, V., Haas, R., Mösta, P., & Shapiro, S. L. 2015, CQGra, 32, 175009
Fernández, R., Foucart, F., Kasen, D., et al. 2017, CQGra, 34, 154001
Fernández, R., & Metzger, B. D. 2013a, MNRAS, 435, 502
Fernández, R., & Metzger, B. D. 2013b, ApJ, 763, 108
Fernández, R., Quataert, E., Schwab, J., Kasen, D., & Rosswog, S. 2015, MNRAS, 449, 390
Fishbone, L. G., & Moncrief, V. 1976, ApJ, 207, 962
Foucart, F., Duez, M. D., Kidder, L. E., et al. 2018, PhRvD, 98, 063007
Foucart, F., O'Connor, E., Roberts, L., et al. 2015, PhRvD, 91, 124021
Foucart, F., O'Connor, E., Roberts, L., et al. 2016, PhRvD, 94, 123016
Freiburghaus, C., Rosswog, S., & Thielemann, F. K. 1999, ApJL, 525, L121
Fujibayashi, S., Sekiguchi, Y., Kiuchi, K., & Shibata, M. 2017, ApJ, 846, 114
Galeazzi, F., Kastaun, W., Rezzolla, L., & Font, J. A. 2013, PhRvD, 88, 064009
Gammie, C. F., McKinney, J. C., & Tóth, G. 2003, ApJ, 589, 444
Gourgoulhon, E., Grandclément, P., Marck, J.-A., Novak, J., & Taniguchi, K. 2016, LORENE: Spectral Methods Differential Equations Solver, Astrophysics Source Code Library, ascl:1608.018
Grossman, D., Korobkin, O., Rosswog, S., & Piran, T. 2014, MNRAS, 439, 757
Hawley, J. F., Guan, X., & Krolik, J. H. 2011, ApJ, 738, 84
Hawley, J. F., Richers, S. A., Guan, X., & Krolik, J. H. 2013, ApJ, 772, 102
Hossein Nouri, F., Duez, M. D., Foucart, F., et al. 2018, PhRvD, 97, 083014
Houck, J. C., & Chevalier, R. A. 1991, ApJ, 376, 234
Janiuk, A. 2014, A&A, 568, A105
Janiuk, A. 2019, ApJ, 882, 163
Janiuk, A., Mioduszewski, P., & Moscibrodzka, M. 2013, ApJ, 776, 105
Just, O., Goriely, S., Janka, H.-T., Nagataki, S., & Bauswein, A. 2021, arXiv:2102.08387
Just, O., Obergaulinger, M., & Janka, H. T. 2015, MNRAS, 453, 3386
Kasen, D., Badnell, N. R., & Barnes, J. 2013, ApJ, 774, 25
Kasen, D., & Barnes, J. 2019, ApJ, 876, 128
Kasen, D., Fernández, R., & Metzger, B. D. 2015, MNRAS, 450, 1777
Kasen, D., Metzger, B., Barnes, J., Quataert, E., & Ramirez-Ruiz, E. 2017, Natur, 551, 80
Kasliwal, M. M., Kasen, D., Lau, R. M., et al. 2019, MNRAS, in press
Kilpatrick, C. D., Foley, R. J., Kasen, D., et al. 2017, Sci, 358, 1583
Kiuchi, K., Kyutoku, K., Sekiguchi, Y., & Shibata, M. 2018, PhRvD, 97, 124039
Kiuchi, K., Kyutoku, K., Sekiguchi, Y., Shibata, M., & Wada, T. 2014, PhRvD, 90, 041502
Kiuchi, K., Sekiguchi, Y., Kyutoku, K., et al. 2015, PhRvD, 92, 064034
Kohri, K., & Mineshige, S. 2002, ApJ, 577, 311
Kulkarni, S. R. 2005, arXiv:astro-ph/0510256
Lee, W. H., & Ramirez-Ruiz, E. 2007, NJPh, 9, 17
Lee, W. H., Ramirez-Ruiz, E., & López-Cámara, D. 2009, ApJL, 699, L93
Lee, W. H., Ramirez-Ruiz, E., & Page, D. 2004, ApJL, 608, L5
Lee, W. H., Ramirez-Ruiz, E., & Page, D. 2005, ApJ, 632, 421
Li, L.-X., & Paczyński, B. 1998, ApJL, 507, L59
Li, X., & Siegel, D. M. 2021, PhRvL, 126, 251101
Lippuner, J., Fernández, R., Roberts, L. F., et al. 2017, MNRAS, 472, 904

Lippuner, J., & Roberts, L. F. 2015, ApJ, 815, 82
Liu, T., Gu, W.-M., & Zhang, B. 2017, NewAS, 79, 1
Margalit, B., & Metzger, B. D. 2017, ApJL, 850, L19
Martin, D., Perego, A., Arcones, A., et al. 2015, ApJ, 813, 2
Metzger, B. D. 2019, LRR, 23, 1
Metzger, B. D., Arcones, A., Quataert, E., & Martínez-Pinedo, G. 2010, MNRAS, 402, 2771
Metzger, B. D., & Fernández, R. 2014, MNRAS, 441, 3444
Metzger, B. D., Piro, A. L., & Quataert, E. 2008, MNRAS, 390, 781
Miller, J. M., Ryan, B. R., & Dolence, J. C. 2019a, ApJS, 241, 30
Miller, J. M., Ryan, B. R., Dolence, J. C., et al. 2019b, PhRvD, 100, 023008
Miller, J. M., Sprouse, T. M., Fryer, C. L., et al. 2020, ApJ, 902, 66
Murguia-Berthier, A., Ramirez-Ruiz, E., Kilpatrick, C. D., et al. 2017, ApJL, 848, L34
Nakar, E. 2007, PhR, 442, 166
Nakar, E. 2020, PhR, 886, 1
Narayan, R., Paczynski, B., & Piran, T. 1992, ApJL, 395, L83
Narayan, R., Piran, T., & Kumar, P. 2001, ApJ, 557, 949
Nedora, V., Bernuzzi, S., Radice, D., et al. 2021, ApJ, 906, 98
Neilsen, D., Liebling, S. L., Anderson, M., et al. 2014, PhRvD, 89, 104029
Nicholl, M., Berger, E., Kasen, D., et al. 2017, ApJL, 848, L18
Noble, S. C., Gammie, C. F., McKinney, J. C., & Del Zanna, L. 2006, ApJ, 641, 626
Noble, S. C., Krolik, J. H., & Hawley, J. F. 2009, ApJ, 692, 411
Noble, S. C., Krolik, J. H., & Hawley, J. F. 2010, ApJ, 711, 959
Noble, S. C., Mundim, B. C., Nakano, H., et al. 2012, ApJ, 755, 51
O'Connor, E., & Ott, C. D. 2010, CQGra, 27, 114103
Palenzuela, C., Liebling, S. L., Neilsen, D., et al. 2015, PhRvD, 92, 044045
Perego, A., Rosswog, S., Cabezón, R. M., et al. 2014, MNRAS, 443, 3134
Pian, E., D'Avanzo, P., Benetti, S., et al. 2017, Natur, 551, 67
Popham, R., Woosley, S. E., & Fryer, C. 1999, ApJ, 518, 356
Powell, M. J. D. 1970, in A New Algorithm for Unconstrained Optimization, ed. J. B. Rosen, O. L. Mangasarian, & K. Ritter (New York: Academic Press), 31
Press, W. H., Teukolsky, S. A., Vetterling, W. T., & Flannery, B. P. 1992, Numerical Recipes in C (2nd ed.; Cambridge: Cambridge Univ. Press)
Radice, D., Bernuzzi, S., & Perego, A. 2020, ARNPS, 70, 95
Radice, D., Galeazzi, F., Lippuner, J., et al. 2016, MNRAS, 460, 3255
Radice, D., Perego, A., Hotokezaka, K., et al. 2018, ApJ, 869, 130
Ravi, V., & Lasky, P. D. 2014, MNRAS, 441, 2433
Roberts, L. F., Kasen, D., Lee, W. H., & Ramirez-Ruiz, E. 2011, ApJL, 736, L21
Roberts, L. F., Lippuner, J., Duez, M. D., et al. 2017, MNRAS, 464, 3907
Rosswog, S., Feindt, U., Korobkin, O., et al. 2017, CQGra, 34, 104001
Rosswog, S., & Liebendörfer, M. 2003, MNRAS, 342, 673
Rosswog, S., Liebendörfer, M., Thielemann, F. K., et al. 1999, A&A, 341, 499
Ruffert, M., Janka, H. T., & Schaefer, G. 1996, A&A, 311, 532
Ruiz, M., Lang, R. N., Paschalidis, V., & Shapiro, S. L. 2016, ApJL, 824, L6
Ruiz, M., Shapiro, S. L., & Tsokaros, A. 2018, PhRvD, 97, 021501
Sano, T., Inutsuka, S.-i., Turner, N. J., & Stone, J. M. 2004, ApJ, 605, 321
Schneider, A. S., Roberts, L. F., & Ott, C. D. 2017, PhRvC, 96, 065802
Shappee, B. J., Simon, J. D., Drout, M. R., et al. 2017, Sci, 358, 1574
Shibata, M., & Taniguchi, K. 2006, PhRvD, 73, 064027
Siegel, D. M. 2019, EPJA, 55, 203
Siegel, D. M., Barnes, J., & Metzger, B. D. 2019, Natur, 569, 241
Siegel, D. M., Ciolfi, R., & Rezzolla, L. 2014, ApJL, 785, L6
Siegel, D. M., & Metzger, B. D. 2017, PhRvL, 119, 231102
Siegel, D. M., & Metzger, B. D. 2018, ApJ, 858, 52
Siegel, D. M., Mösta, P., Desai, D., & Wu, S. 2018, ApJ, 859, 71
Smartt, S. J., Chen, T. W., Jerkstrand, A., et al. 2017, Natur, 551, 75
Soares-Santos, M., Holz, D. E., Annis, J., et al. 2017, ApJL, 848, L16
Sorathia, K. A., Reynolds, C. S., Stone, J. M., & Beckwith, K. 2012, ApJ, 749, 189
Tanaka, M., & Hotokezaka, K. 2013, ApJ, 775, 113
Tanvir, N. R., Levan, A. J., González-Fernández, C., et al. 2017, ApJL, 848, L27
Villar, V. A., Guillochon, J., Berger, E., et al. 2017, ApJL, 851, L21
Zalamea, I., & Beloborodov, A. M. 2011, MNRAS, 410, 2302
Zenati, Y., Perets, H. B., & Toonen, S. 2019, MNRAS, 486, 1805
Zilhão, M., & Noble, S. C. 2014, CQGra, 31, 065013